Serration Phenomena Occurring During Tensile Tests of Three High-Manganese Twinning-Induced Plasticity (TWIP) Steels

SEOKMIN HONG, SANG YONG SHIN, JUNGHOON LEE, DONG-HYUN AHN, HYOUNG SEOP KIM, SUNG-KYU KIM, KWANG-GEUN CHIN, and SUNGHAK LEE

In this study, the serration phenomena of two high-Mn TWIP steels and an Al-added TWIP steel were examined by tensile tests, and were explained by the microstructural evolution including formation of localized Portevin–Le Chatelier deformation bands and twins. In stress–strain curves of the high-Mn steels, serrations started in a fine and short shape, and their height and periodic interval increased with increasing strain, whereas the Al-added steel did not show any serrations. According to digital images of strain rate and strain obtained from a vision strain gage system, deformation bands were initially formed at the upper region of the gage section, and moved downward along the tensile loading direction. The time when the band formation started was matched with the time when one serration occurred in the stress–time curve. This serration behavior was generally explained by dynamic strain aging, which was closely related with the formation of deformation bands.

DOI: 10.1007/s11661-013-2007-1

I. INTRODUCTION

IN automotive industries, many efforts for decreasing CO_2 emission and increasing fuel efficiency have been conducted on highly deformable steel sheets such as transformation-induced plasticity (TRIP) steels and twinning-induced plasticity (TWIP) steels. Particularly in TWIP steels, mechanical twins are formed during deformation, and prevent the dislocation movement as they play a role in refining grains, which is known to be Hall–Petch effect.[1–6] Since the necking is also suppressed because of high work hardening rate, TWIP steels show high strength and ductility simultaneously.[6–9]

In general, a considerable amount (about 20 wt pct) of Mn is contained in TWIP steels composed of austenite.[6] Their active commercialization has been postponed because they are easily subjected to the cracking during forming or to the delayed fracture after forming.[6,10–14] According to the stabilization of austenite at room temperature and the sufficient formation of twins, however, the reduction in Mn content is somewhat difficult. Recently, TWIP steels containing Al have been developed to improve the formability and to prevent the delayed fracture. Here, Al plays an important role in decreasing twin formation because it works for increasing stacking fault energy.[15–20] These Al-added TWIP steels have excellent formability due to the increase in slip and the decrease in twin formation.

Chin *et al.*[10] reported that cracks were formed during cup forming of a high-Mn TWIP steel, whereas they were not found in an Al-added TWIP steel, and explained the cracking behavior by the stress concentration on a cup side of the high-Mn steel. Berrahmoune *et al.*[21] found the delayed fracture after deep drawing of 301LN austenite steels, and explained it by the localization of residual stresses. However, detailed mechanisms of cracking or delayed fracture are not sufficiently understood in relation to microstructures.

In addition, TWIP steels show a peculiar characteristic of serration phenomenon occurring during tensile deformation.[6,15,22–25] This serration is generally explained by dynamic strain aging (DSA),[26–29] by which localized Portevin–Le Chatelier (PLC) deformation bands are formed.[6,22–24] The DSA is closely related with interactions between C atoms and dislocations. When the diffusion rate of C atoms is faster than the moving velocity of dislocations, C atoms are stuck again to mobile dislocations, and obstruct the movement of dislocations.[26] In conventional low-carbon plain carbon steels, there exists a temperature range of the DSA because the diffusion rate of C atoms and mobility of dislocations are varied with strain rate and temperature.[26,27] The DSA generally occurs above 373 K (100 °C). In the initial stage of deformation, it hardly occurs because it needs a considerable amount of dislocations. In TWIP steels, however, serrations are found even at room temperature, at which the diffusion

SEOKMIN HONG, Postdoctoral Research Associate, JUNGHOON LEE, and DONG-HYUN AHN, Research Assistants, are with the Center for Advanced Aerospace Materials, Pohang University of Science and Technology, Pohang, 790-784, Korea. SANG YONG SHIN, Assistant Professor, is with the School of Materials Science and Engineering, University of Ulsan, Ulsan, 680-719, Korea. HYOUNG SEOP KIM and SUNGHAK LEE, Professors, are with the Center for Advanced Aerospace Materials, Pohang University of Science and Technology, and also with the Materials Science and Engineering, Pohang University of Science and Technology, Pohang, 790-784, Korea. Contact e-mail: shlee@postech.ac.kr SUNG-KYU KIM, Senior Principal Researcher, and KWANG-GEUN CHIN, Senior Vice President, are with the HIMASS Research Project Team, Technical Research Laboratories, POSCO, Gwangyang, 545-711, Korea.

Manuscript submitted October 19, 2012.
Article published online September 27, 2013

rate of C atoms are not fast, and even in the initial stage of deformation. Thus, the DSA or serration phenomenon in TWIP steels cannot be simply presented by the existing theory of interactions between C atoms and dislocations.

Since serrations are not found in TWIP steels where C is not contained,[11,12,30–33] they are clearly related with C atoms. C atoms form Mn-C pairs by the strong cohesive interaction with Mn atoms,[34] and form short range ordering (SRO) or short range clustering (SRC) at octahedral sites when the Mn content is high.[35] The SRO or SRC obstructs the movement of dislocations, and thus requires the higher stress for moving dislocations.[36–38] According to Dastur and Leslie,[39] the DSA in Hadfield steels was caused by the reorientation of C atoms of Mn-C pairs after their infiltration into dislocation cores. Owen *et al.*[35] insisted from a local order model that the flow stress due to the DSA increased with increasing number of Mn-C pairs. However, the above explanations on DSA do not consider the formation of twins and dislocation dissociation occurring in TWIP steels as well as the difficulty in diffusion of C atoms at room temperature. In addition, the reason why serrations do not take place in Al-added TWIP steels is not presented, and the microstructural modification processes during tensile deformation or cup forming are not analyzed in detail. From understandings of effects of Al addition on serrations in TWIP steels, it is possible to improve the cup formability or to prevent the delayed fracture.

Microstructures, tensile properties, and cup formability of two high-Mn TWIP steels and an Al-added TWIP steel were investigated in this study. The serration behavior was examined by tensile tests, after which the microstructural modification including the formation of twins was analyzed by electron back-scatter diffraction (EBSD). Deformation bands formed in the tensile specimen were analyzed by a vision strain gage system in detail, which could explain deformation mechanisms related to the microstructural evolution. Based on the results of microstructural evolution and deformation band formation, effects of Al addition on serrations were verified.

II. EXPERIMENTAL PROCEDURE

Three TWIP steels were fabricated by a vacuum induction melting method, and their chemical compositions are 0.6C-18Mn, 0.6C-22Mn, and 0.6C-18Mn-2Al. For convenience, these steels are referred to as "18Mn," "22Mn," and "18Mn2Al," respectively. In the 18Mn2Al steel, 2 wt pct of Al is added to increase the stacking fault energy.[15–17] After thick plates of 30 mm in thickness were homogenized at 1423 K (1150 °C) for 1 hour, they were hot-rolled at 1373 K (1100 °C). The finish rolling temperature was 1173 K (900 °C). The hot-rolled steel sheets of 2.5 mm in thickness were water-cooled to 723 K (450 °C), rolled at this temperature to make 1.2-mm thick sheets, held at 1073 K (800 °C) for 0.5 minute, and water-quenched.

Plate-type tensile specimens (gage length; 30 mm, gage width; 5 mm, gage thickness; 1.2 mm) were prepared in the longitudinal direction. They were tested at room temperature at a strain rate of 1.0×10^3 s^{-1} by a universal testing machine (model; Instron 5582, Instron Corp., Canton, MA, USA) of 98 kN capacity. In order to investigate the tensile deformation behavior, the deformed or fractured specimens were observed by a field emission scanning electron microscope (FE-SEM, model; XL30S FEG, Philips FEI, USA). EBSD analysis was conducted on the deformed specimen by an FE-SEM. The data were interpreted by orientation imaging microscopy (OIM) analysis software provided by TexSEM Laboratories, Inc. Cup forming tests were conducted on steel sheet disks (diameter; 100 mm, thickness; 1.2 mm) under a load of 19.6 kN by a universal sheet and strip metal testing machine (model; USM-50-2, Tokyo Testing Machine Manufacturing, Tokyo, Japan) of 490 kN capacity. The diameter of an extrusion die, extrusion distance, drawing ratio, and extrusion rate were 53.88, 50, 1.8 to 2.0, and 60 mm min^{-1}, respectively.

During the tensile tests, strain rates and strains were measured by a vision strain gage system (model; ARAMIS v6.1, GOM Optical Measuring Techniques, Germany), which could detect three-dimensional coordinates of a deforming specimen surface on the basis of digital image processing delivering three-dimensional displacement and strain. This ARAMIS system recognized the surface structure in digital camera images, and allocated coordinates to image pixels. The first image in the measuring specimen represented the undeformed state, and further images were recorded during the deformation. The vision strain gage system compared the digital images, and calculated the displacement and strain. The local displacement, strain, and strain rate according to the position from the base line (the lower part of the gage section) were measured along the center line of the gage section. Then, the strain, strain rate, width, and moving velocity of deformation bands formed in the gage section were investigated in detail during the tensile deformation.

III. RESULTS

A. *Tensile Properties and Cup Formability*

Figure 1(a) shows room-temperature engineering stress–strain curves of the three TWIP steels, from which yield strengths, ultimate tensile strengths, and elongations are measured, as listed in Table I. From these curves, true stress–strain curves and strain hardening rate curves were also drawn, as shown in Figure 1(b). The 18Mn steel has the yield strength, ultimate tensile strength, and elongation of 452, 1114 MPa, and 60.1 pct, respectively. It shows a relatively high strain hardening, together with serration in stress–strain curve. The serration starts in a fine and short shape, and its height and periodic interval increase with increasing strain (Figures 1(a) and (b)). With increasing Mn content, the yield and ultimate tensile

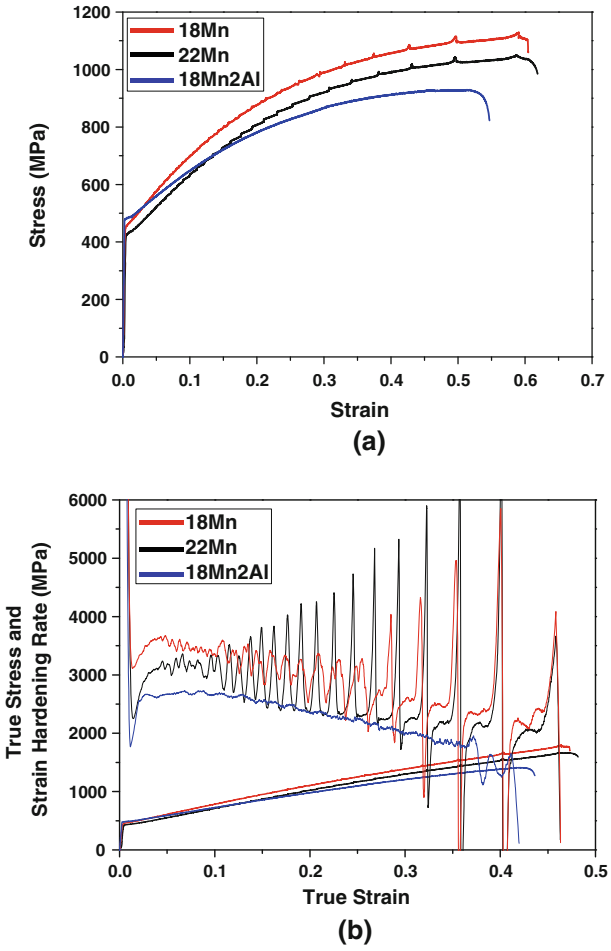

Fig. 1—Room-temperature (*a*) engineering stress–strain curves and (*b*) true stress–true strain curves and strain hardening rate curves of the three TWIP steels.

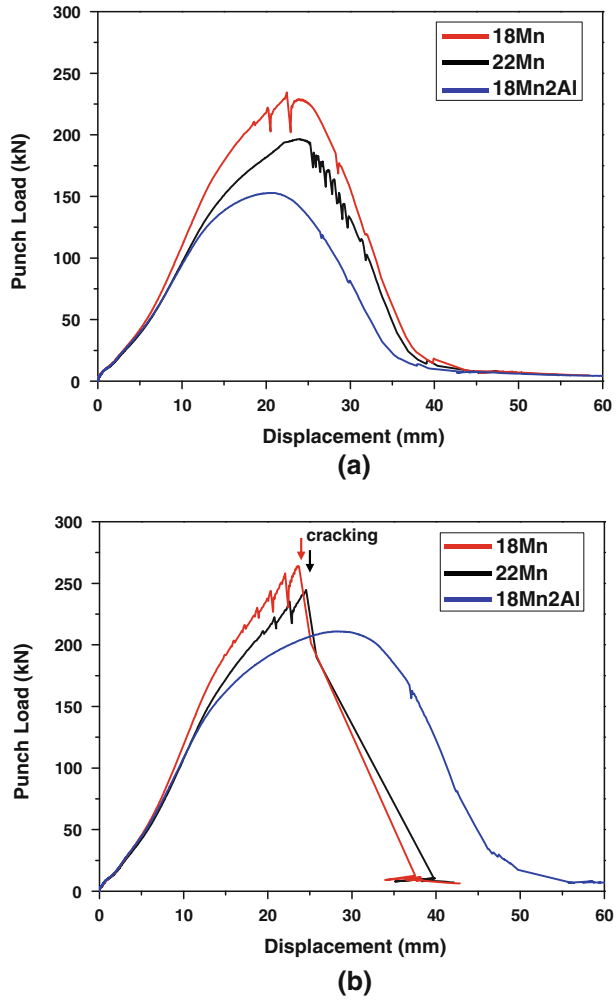

Fig. 2—Punch load–displacement curves of the cup forming test at the drawing ratio of (*a*) 1.8 and (*b*) 2.0 for the three TWIP steels.

Table I. Room-Temperature Tensile Properties of the TWIP Steels

Steel	Yield Strength (MPa)	Ultimate Tensile Strength (MPa)	Elongation (Pct)
18Mn	452	1114	60.1
22Mn	425	1039	62.1
18Mn2Al	477	929	54.6

strengths decrease, while the elongation is hardly varied. Overall serration behavior of the 22Mn steel is similar to that of the 18Mn steel, while the fluctuation of strain hardening rate is more severe. As Al is added, the ultimate tensile strength, elongation, and the strain hardening decrease, while the yield strength increases slightly. In the 18Mn2Al steel, the serration almost disappears.

Figures 2(a) and (b) show punch load–displacement curves of the cup forming tests, when drawing ratios are 1.8 and 2.0, respectively. No cracks were found after the punching with a drawing ratio of 1.8. The punch load increases with increasing displacement, reaches the peak load point, and then decreases (Figure 2(a)). Though the three steels show the similar cup forming behavior, some fluctuations take place in the 18Mn and 22Mn steels, like in the case of serrations in tensile stress–strain curves. The peak load is highest in the 18Mn steel, and decreases in the order of the 22Mn and 18Mn2Al steels. This indicates that the lower load is needed for the cup forming when Mn or Al is added, and that the cup forming results can be explained by the extent of strain hardening. The 18Mn and 22Mn steels having higher strain hardening need the higher punch load during the cup forming tests, whereas the 18Mn2Al steel having lower strain hardening needs the lower load, because the punch load increases with increasing strain hardening. After the punching with a drawing ratio of 2.0, cracks were found in the 18Mn and 22Mn steels, whereas they were not in the 18Mn2Al steel. The peak load decreases in the order of the 18Mn, 22Mn, and 18Mn2Al steels, like in the case of the drawing ratio of 1.8, but the displacements of the 18Mn and 22Mn steels are seriously reduced as fluctuations appear before the peak load (Figure 2(b)).

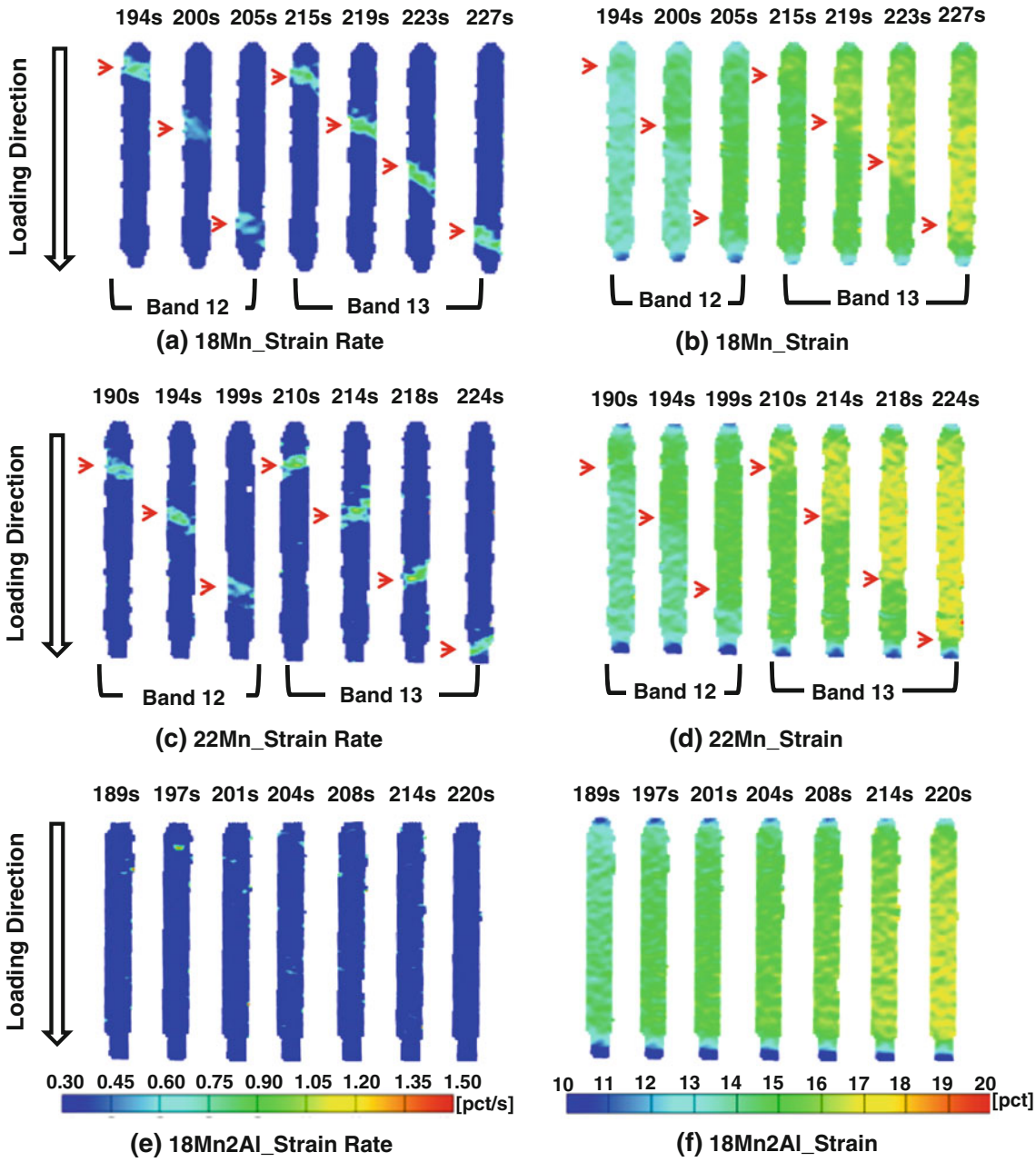

Fig. 3—Digital images of strain rate and strain obtained from the vision strain gage system in the former stage of tensile deformation for the (*a*) and (*b*) 18Mn, (*c*) and (*d*) 22Mn, and (*e*) and (*f*) 18Mn2Al steels. The number of deformation bands and the time at the deformation band formation are marked on each digital image of strain rate and strain. Deformation bands are initially formed at the upper region of the gage section, and move downward along the tensile loading direction as marked by arrows. In the 18Mn2Al steel, deformation bands are not found.

B. *Observation of Tensile Deformation Behavior*

In order to observe the relation between serration and deformation band formation, the vision strain gage system was simultaneously used with the tensile tests. Figures 3, 4, and 5 show digital images of strain rate and strain in the former, latter, and final stages of tensile deformation, respectively. The number of deformation bands and the time when the bands are formed are marked on each digital image. They are also marked on stress–time curves in the former, latter, and final stages of tensile deformation, as shown in Figures 6(a) through (c), respectively.

In the former stage, deformation bands, whose strain rates are higher than the other region, are clearly visible in digital images of strain rate of the 18Mn steel, as they are colored in light blue (arrow marks in Figure 3(a)). These deformation bands indicate the area of severely strained localization. It is initially formed at the upper region of the gage section, and moves downward along the tensile loading direction. The time when the band

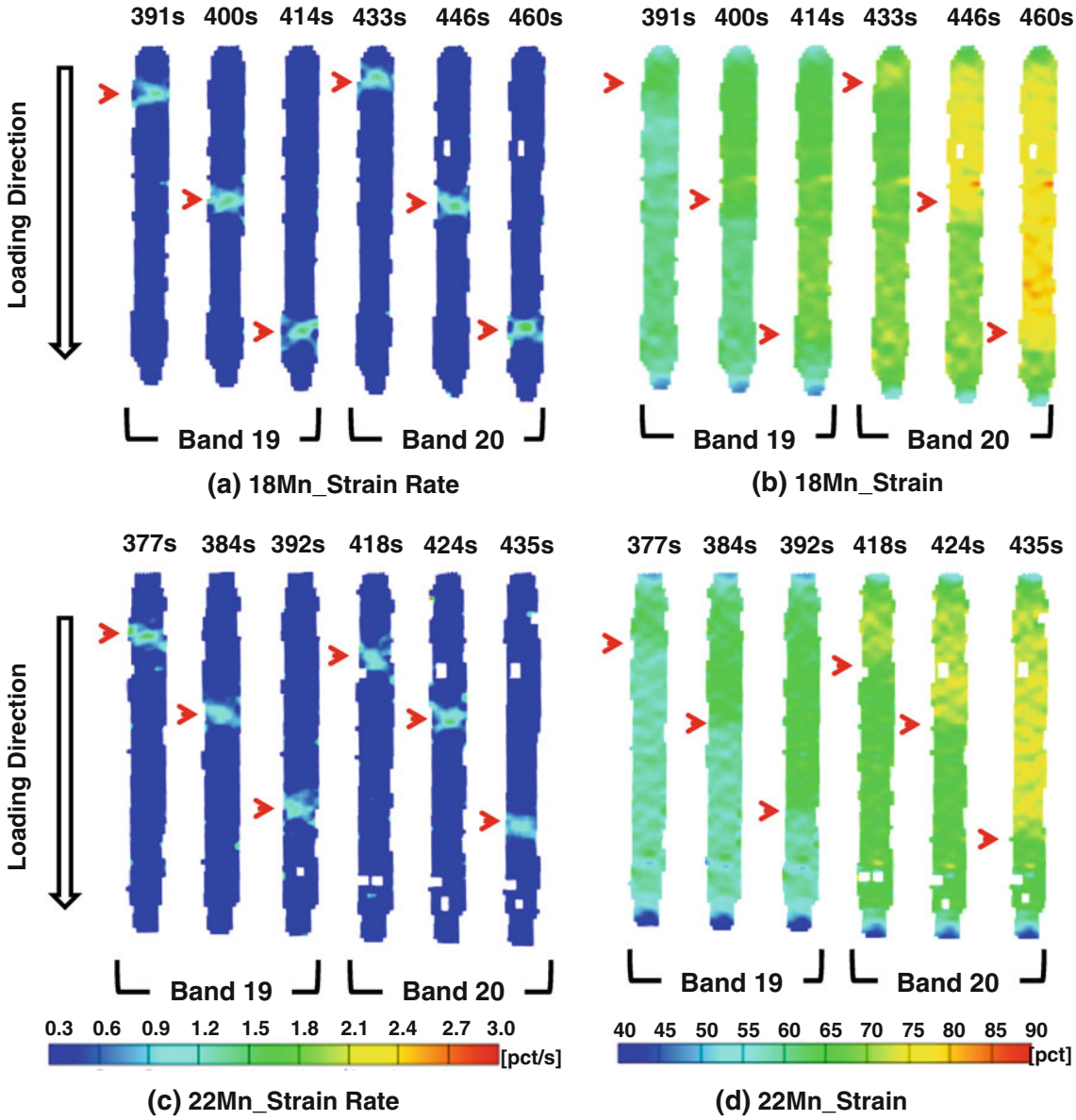

Fig. 4—Digital images of strain rate and strain obtained from the vision strain gage system in the latter stage of tensile deformation for the (*a*) and (*b*) 18Mn and (*c*) and (*d*) 22Mn steels. The number of deformation bands and the time at the deformation band formation are marked on each digital image of strain rate and strain.

formation starts is well matched with the time when one serration occurs in the stress–time curve of Figure 6(a). For example, the 12th band moves down during the time of 194 to 205 seconds (Figure 3(a)), which is matched with the time of 193 seconds when the 12th serration takes place in the stress–time curve (Figure 6(a)), because the band formation starts just before the first detect time of digital image (194 seconds). After the 12th band disappears, a new band, the 13th band, is formed again at the upper region of the gage section, and moves down during the time of 215 to 227 seconds. Here again, the time when the band formation starts is matched with the time of the 13th serration (213 seconds). In digital images of strain (Figure 3(b)), bands are hardly observable, unlike in the case of digital images of strain rate. The average strain is 13 to 14 pct at the time of the 12th band formation, which can be roughly proved in digital images of strain (Figure 3(b)), and tends to increase up to about 15 pct at the time of the next 13th band formation. It is found that the strain is somewhat higher in the region above arrows (band passed) than in the region below arrows (band not passed). This implies that the overall strain increases as the band moves downward. In the 22Mn steel, bands are well formed and moved downward, like in the 18Mn steel (Figures 3(c) and (d) and 6(a)). In the 18Mn2Al steel, on the other hand, bands are not formed as the deformation occurs homogeneously (Figures 3(e) and (f)). Thus, the serration does not occur in the stress–time curve (Figure 6(a)).

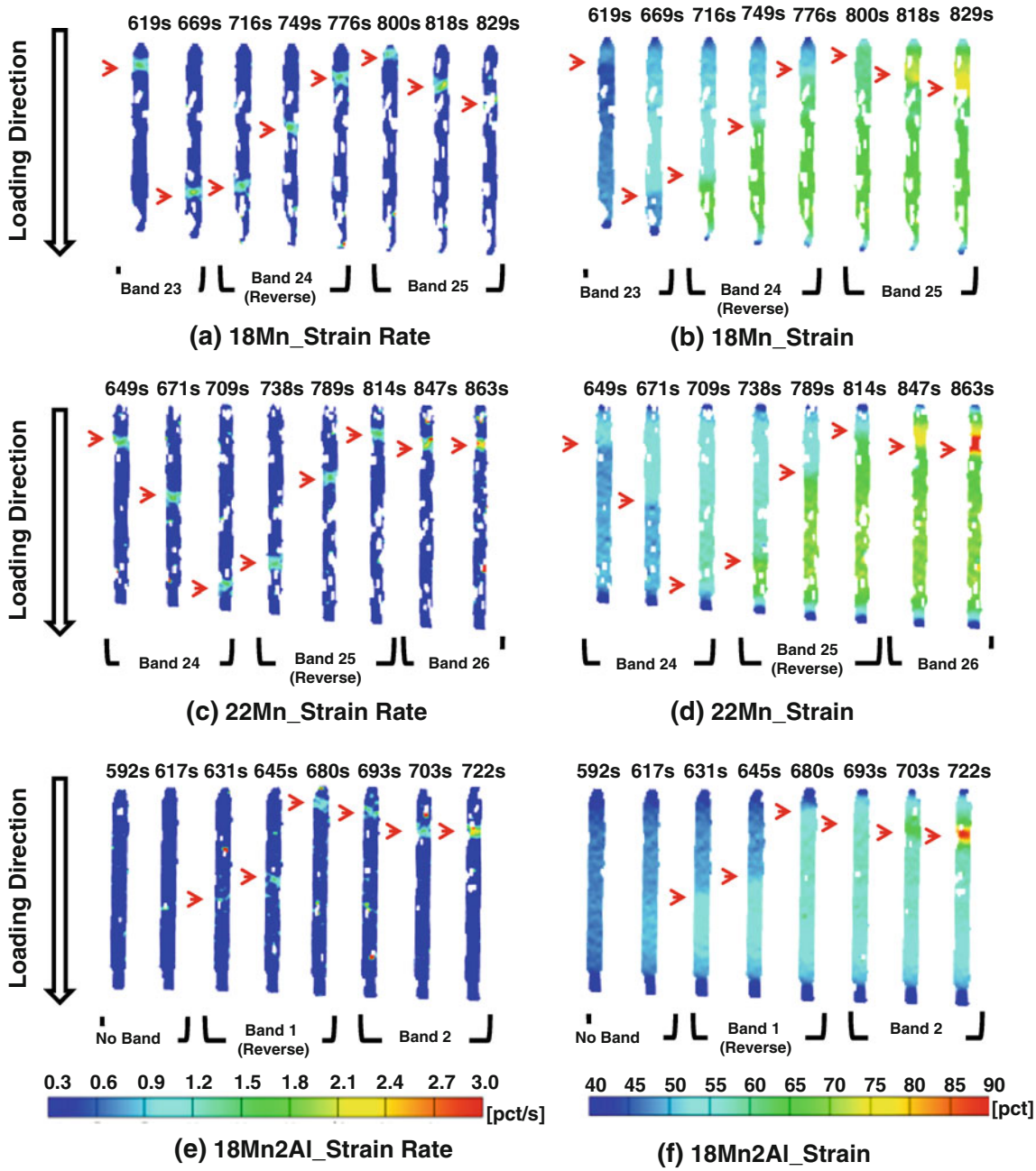

Fig. 5—Digital images of strain rate and strain obtained from the vision strain gage system in the final stage of tensile deformation for the (*a*) and (*b*) 18Mn, (*c*) and (*d*) 22Mn, and (*e*) and (*f*) 18Mn2Al steels. The number of deformation bands and the time at the deformation band formation are marked on each digital image of strain rate and strain. The 2nd last deformation band moves upward, and the last band moves downward to reach the fracture.

In the latter stage of tensile deformation, bands are also formed in the 18Mn and 22Mn steels, as shown in digital images of strain rate of Figures 4(a) and (c), whereas they are not formed in the 18Mn2Al steel. Overall strain rate and strain levels are higher than those of the former stage (Figures 4(a) through (d)), and the periodic interval of band formation or serration is larger than that of the former stage (Figure 6(b)). However, overall serration behavior in the latter stage was similar to that in the former stage.

Digital images of strain rates and strains of the final stage prior to fracture are shown in Figures 5(a) through (f). The formation and movement of deformation bands are well observed, like in the latter stage, and the periodic interval of band formation and overall strain rate and strain levels considerably increase in comparison to those of the latter stage. Even in the 18Mn2Al steel, bands appear in the final stage, as shown in Figures 5(e) and (f). This is confirmed from serrations in the stress–time curve (Figure 6(c)) or the strain hardening rate-true strain

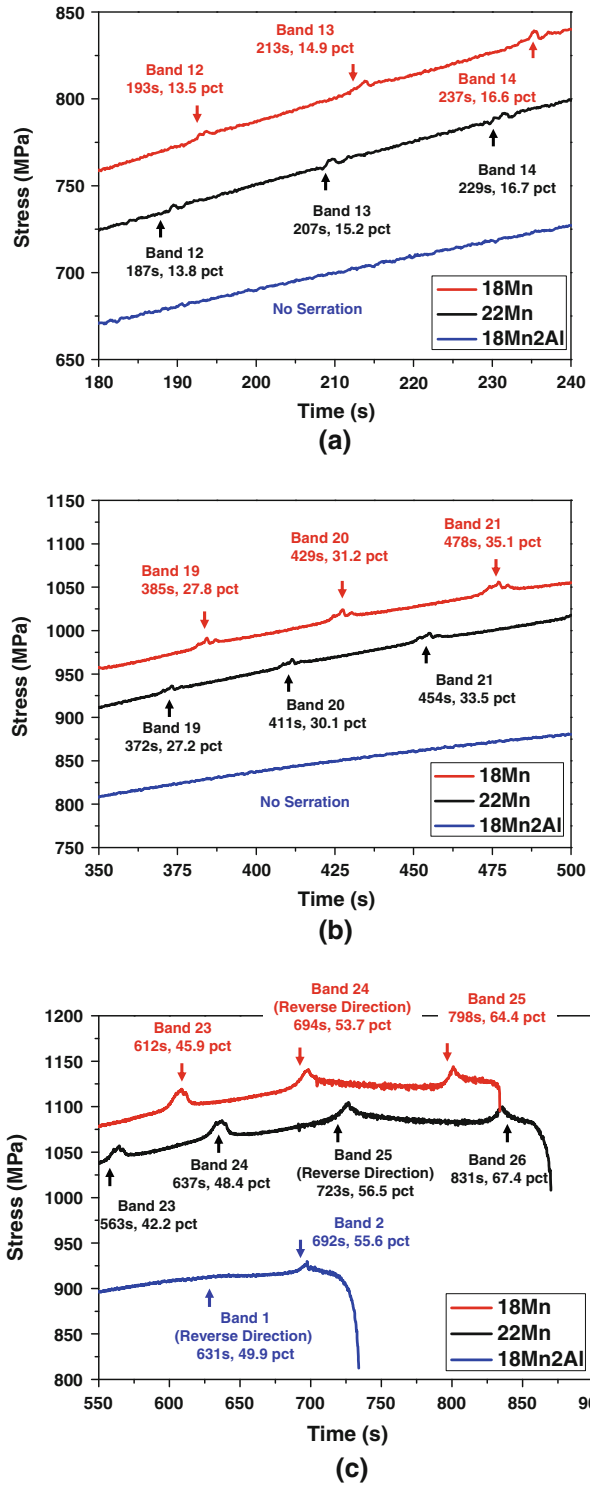

Fig. 6—Stress–time curves in the (*a*) former, (*b*) latter, and (*c*) final stages of tensile deformation of the three steels. The number of deformation bands and the time and strain at the deformation band formation are marked on each serration.

curve (Figure 1(b)), although heights of serrations or fluctuations are small. In all the three steels, the 2nd last band moves upward, and the last band moves downward to reach the fracture (Figures 5(a) through (f)). This result can be confirmed from strain images during the 2nd last band period, in which the strain of the lower part is higher than that of the upper part, as the band moves upward. After the 2nd last band moves upward, the stress–time curves of Figure 6(c) show tiny continuous fluctuations which are somewhat different shapes of serration.

The total number of deformation bands and the stress and strain at which the 1st band is formed were measured from the vision strain gage system, and the results are shown in Table II. The numbers of bands are 25, 26, and 2 in the 18Mn, 22Mn, and 18Mn2Al steels, respectively, as shown in Figures 3 through 6. In the 18Mn and 22Mn steels, bands start to form at low strains of 3.2 to 3.5 pct and stresses of 500 to 520 MPa, while they are formed at considerably high strain of 50 pct and stress of 910 MPa in the 18Mn2Al steel.

In order to investigate the deformation band formation in detail, the strain rate and strain obtained from the vision strain gage system were plotted, as bands move downward along the center line of the gage section. For example, the strain rate and strain data of the 12th band of the 22Mn steel are shown in Figures 7(a) and (b). Here, the base line is set at the lower part of the gage section. As a band formed at the upper part moves downward, the strain rate is varied with the detecting position and time, as shown in Figure 7(a). From this plot, the strain rate and width of band were measured. The band moving velocity (v_B, unit:mm s^{-1}) can be measured from the following relation:

$$v_B = \frac{L_{B2} - L_{B1}}{t_{B2} - t_{B1}}, \qquad [1]$$

where L_B and t_B are the detecting position and time, respectively, of bands. The strain is also varied with the detecting position and time, as shown in Figure 7(b), from which the average strain of bands can be measured. According to the above measurement method, the average strain, strain rate, width, and moving velocity of each band were measured as a function of strain, and the results are shown in Figures 8(a) through (d). In all the plots, total data points are 53 because the numbers of bands are 25, 26, and 2 in the 18Mn, 22Mn, and 18Mn2Al steels, respectively. The average strain of band is quite small in the initial stage of tensile deformation, and increases slightly with increasing strain (Figure 8(a)). When the strain is higher than 50 pct near the final stage, the average strain abruptly increases to reach the fracture. The average strain rate of band almost linearly increases with increasing strain (Figure 8(b)). The average band width rapidly increases below the strain of 15 pct, and then becomes saturated at about 4 mm (Figure 8(c)). Figure 8(d) shows the linearly decreasing trend of average band moving velocity with increasing strain. Here, three data points located below the x axis, as marked by a dotted rectangular area, indicate the backward movement of the 2nd last band in the final stage. This moving velocity data are closely related with the increase in periodic interval of band formation with increasing strain.

Table II. Characteristics of Deformation Bands Formed During the Tensile Deformation of the TWIP Steels

Steel	The Number of Deformation Bands	Stress at 1st Deformation Band Formation (MPa)	Strain at 1st Deformation Band Formation (Pct)
18Mn	25	523	3.3
22Mn	26	502	3.5
18Mn2Al	2	913	49.8

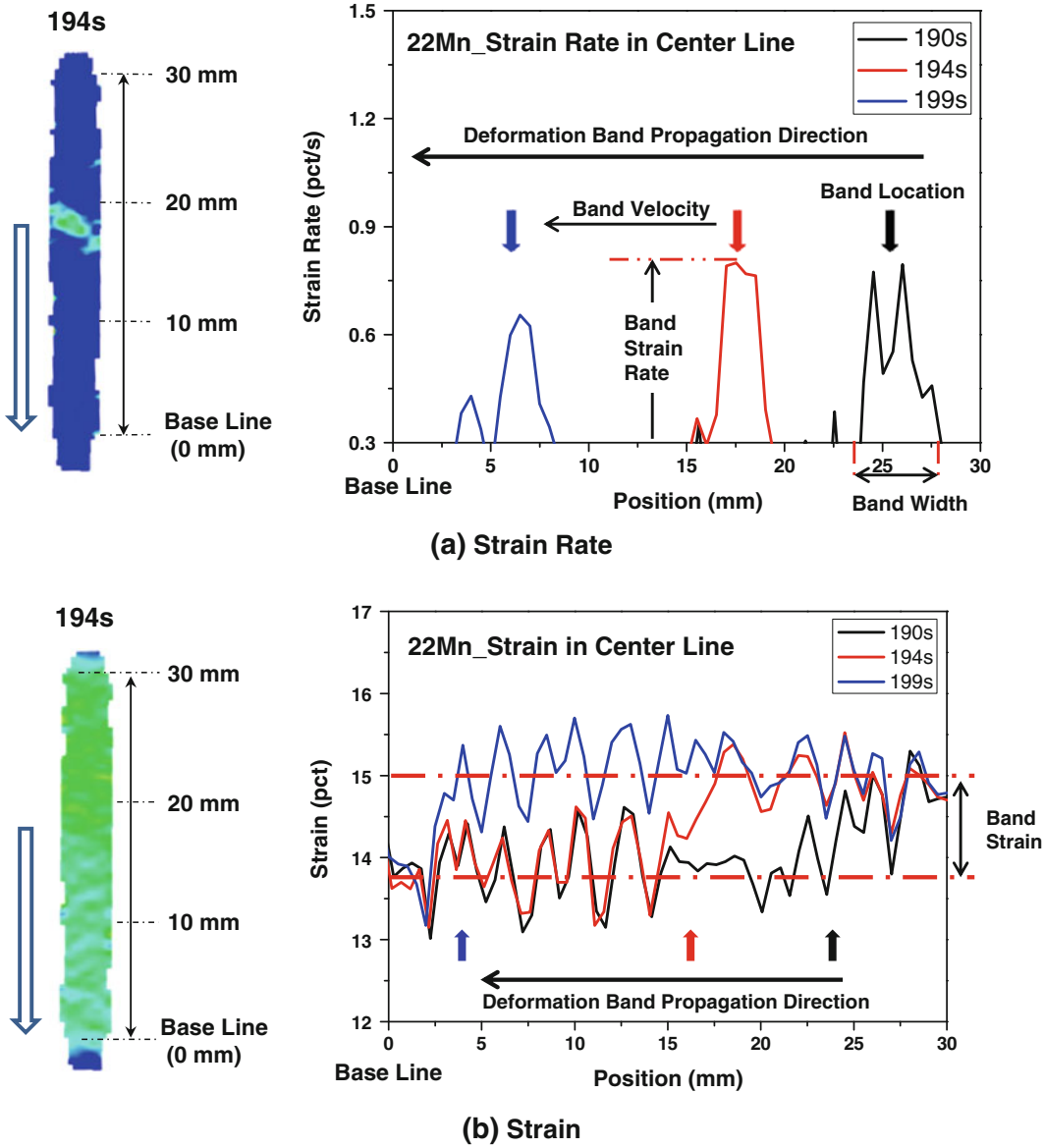

Fig. 7—(*a*) Strain rate and (*b*) strain obtained from the vision strain gage system along the center line of the gage section as a function of position from the base line (the lower part of the gage section) for the 12th band of the 22Mn steel. As a deformation band formed at the upper part moves downward, the strain rate and strain is varied with the detecting position and time in the vision strain gage system.

IV. DISCUSSION

A. *Dynamic Strain Aging (DSA) in TWIP Steels*

In order to explain the DSA in TWIP steels, the dislocation dissociation and twin formation should be considered. C atoms move to tetrahedral sites by the movement of leading partial dislocations or the formation of mechanical twins, and promote the lattice distortion to induce the strengthening.[36,40,41] In high-Mn TWIP steels, C atoms form SRO or SRC.[34,35] It was proposed that leading partials could break the SRO/SRC, thereby allowing C atoms to move to tetrahedral sites.[37–39,42,43] This process requires high stresses, and is believed to be the origin of stress peaks in

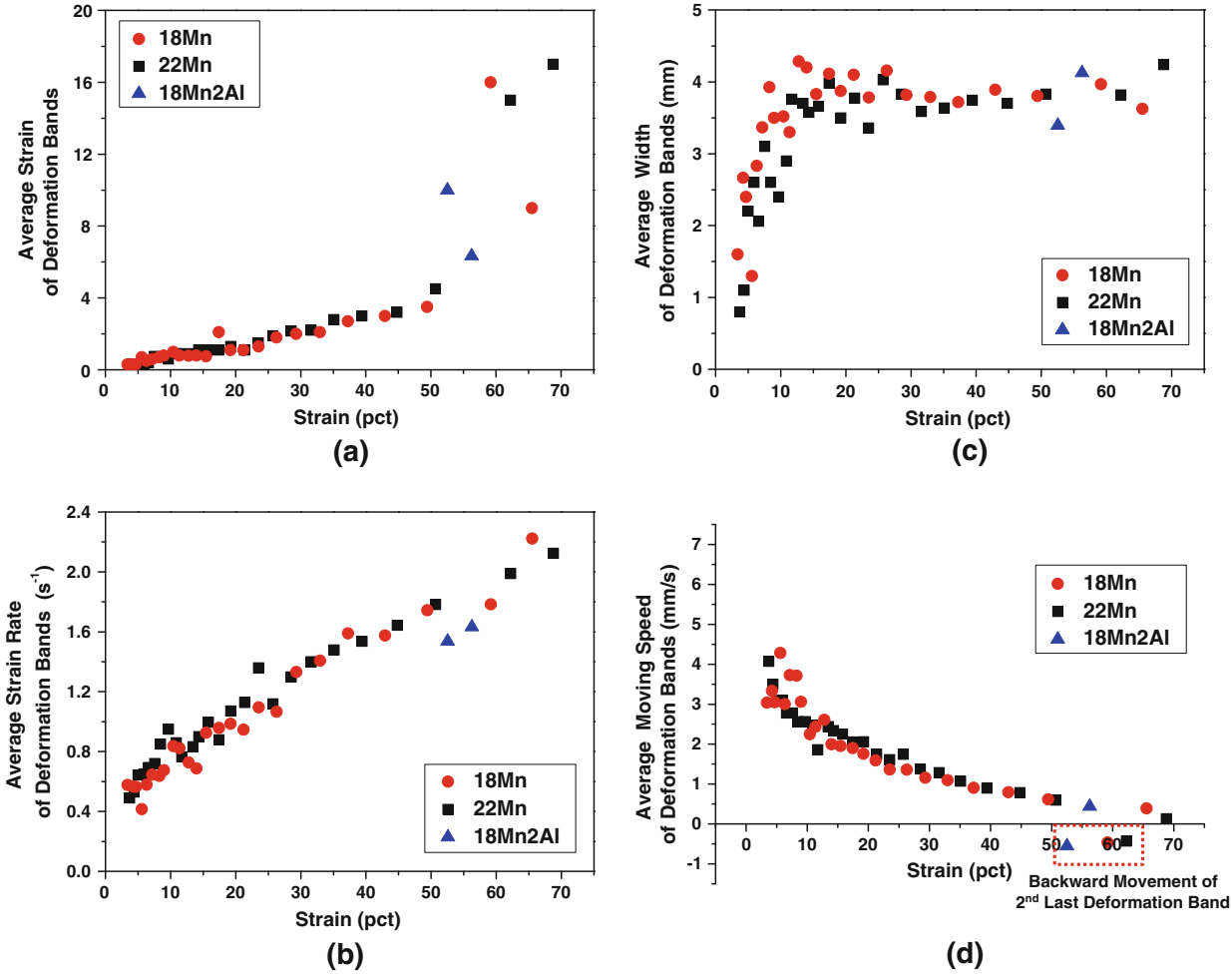

Fig. 8—(*a*) Average strain, (*b*) strain rate, (*c*) width, and (*d*) moving velocity of deformation bands as a function of strain.

Table III. Volume Fraction of Twinned Grains in the TWIP Steels at the Tensile Strain of 20 Pct and Fracture Strain

Steel	At Tensile Strain of 20 Pct (Pct)	At Fracture Strain (Pct)
18Mn	88.1 ± 5.8	92.7 ± 4.5
22Mn	80.2 ± 6.4	90.9 ± 4.3
18Mn2Al	13.0 ± 2.7	81.0 ± 7.3

stress–strain curves. However, if C atoms moved to tetrahedral sites are reoriented again to octahedral sites by the strong interaction with Mn atoms to form Mn-C pairs, the movement of leading partial dislocations is interrupted, which can be a reason of DSA.[39,44]

From other researchers' results,[6,22,39,43,44] it can be speculated that C atoms of Mn-C pairs obstruct the movement of twinning partial (leading partial) dislocations and are easily rearranged to the Mn-C pairs by the strong cohesive interaction with Mn atoms, which leads to the DSA of TWIP steels at room temperature. It means that the formation of twinning partials and Mn-C pairs is closely related with the DSA. Since it is hard to directly observe the Mn-C interaction and dislocation-C interaction using TEM, EBSD, and other experimental equipment, in the present study, the behavior of serration is indirectly observed by changing the Mn and Al contents which can affect the amount of twinning partials and Mn-C pairs. The addition of Mn increases the amount of Mn-C pairs, but it slightly decreases the amount of twinning partials because it increases the stacking fault energy (SFE).[17,18] The addition of Al decreases the amount of twinning partials because it largely increases the SFE (Table III).[15]

The EBSD analysis data (Figures 9(a) through (c)) show that deformation bands are formed after the formation of mechanical twins. In the 22Mn steel, the 1st deformation band appears at the strain of 3.5 pct, while it does at the strain of 3.3 pct in the 18Mn steel. Here, a large number of bands are passed, and its strain hardening rate curve is seriously fluctuated (Table II and Figure 1(b)). This might be because the formation of twinning partials can be slightly delayed, although the interaction between Mn-C pairs and partial dislocations is activated by the increase in Mn-C pairs due to the high-Mn content. In the 18Mn2Al steel, the DSA is tremendously suppressed because the formation of twinning partials is considerably restricted. The movement and reorientation of C atoms are reduced by the addition of Al according to the decrease in carbon

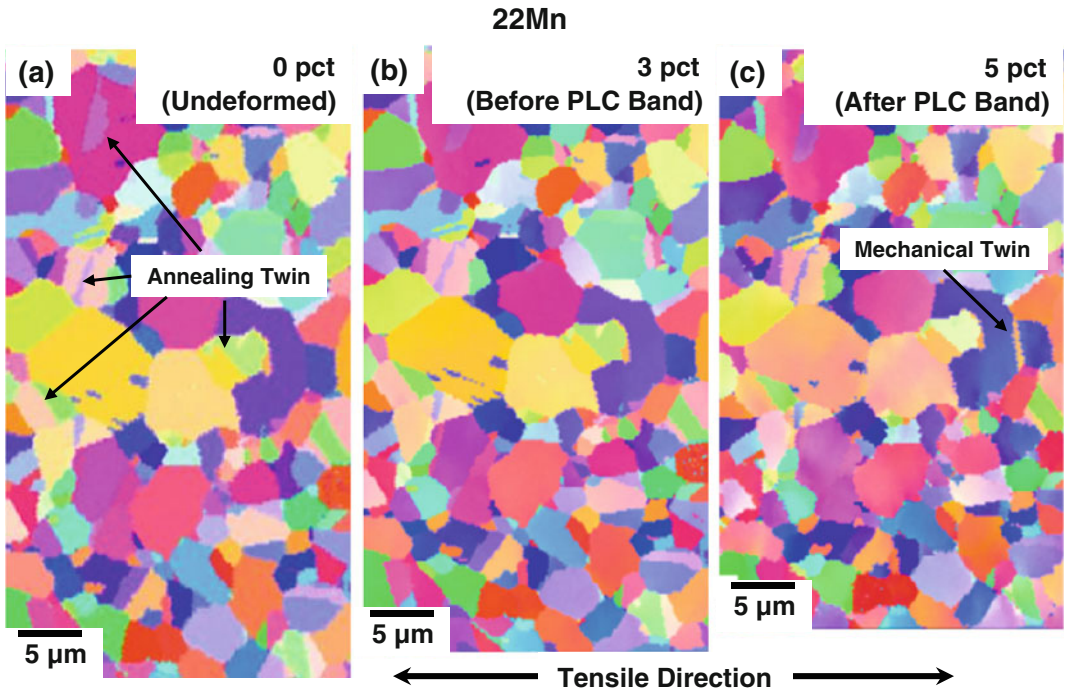

Fig. 9—Inverse pole figure (IPF) color maps of the same observation area after the tensile strain of (*a*) 0 pct (undeformed), (*b*) 3 pct (before the formation of PLC deformation band), and (*c*) 5 pct (after the pass of PLC deformation band) for the 22Mn steel.

activity.[18] These results imply that the interaction between Mn-C pairs and twinning partials is closely related with the DSA. Lee *et al.*[44] also insisted that the single diffusive jump (reorientation) of C atoms of Mn-C pairs and the interaction with stacking faults induced the DSA in TWIP steels even at room temperature. The DSA was observed when the reorientation time of C atoms was shorter than the residence time of stacking faults.[44] Thus, it can be concluded that the reorientation of C atoms of Mn-C pairs obstructs the movement of twinning partial dislocations, thereby resulting in the DSA.

B. *Effect of Mn Addition on Deformation Behavior*

The grain sizes of the 18Mn and 22Mn steels are about 5 μm, and the phase transformation from austenite to ε or α' martensite does not occur, as reported in previous researches.[10,19] The Mn addition into the 18Mn steel slightly lowers the yield and ultimate tensile strengths (Table I) because the amount of dislocation slip and twin formation is varied with stacking fault energy.[17,18] It was reported that the stacking fault energies of the 18Mn and 22Mn steels are 17 and 19 mJ m^{-2}, respectively.[15,45] The increased SFE in the 22Mn steel lowers the strengths by activating the slip deformation, by restraining the twin formation, and by reducing the dynamic Hall–Petch effect.

Figures 10(a) through (c) show SEM micrographs of the 18Mn, 22Mn, and 18Mn2Al steels at the tensile strain of 20 pct and fracture strain. Grains containing twins are less populated in the 22Mn steel than in the 18Mn steel. In the 18Mn2Al steel, only a few twinned grains are observed at the strain of 20 pct, but their volume fraction greatly increases at the fracture strain. From these SEM micrographs, the volume fractions of twined grains were measured, and the results are listed in Table III. The volume fraction of twinned grains is highest in the 18Mn steel at both 20 pct strain and fracture strain, and decreases in the order of the 22Mn and 18Mn2Al steels. The addition of Mn raises the stacking fault energy, and decreases the ultimate tensile strength, while slightly increasing the tensile elongation.

In view of deformation band formation, the addition of Mn raises the number of bands, and lowers the strain at the 1st band formation, as shown in Table II. The height of fluctuations found in the strain hardening rate-true strain curve of Figure 1(b) is also increased. This indicates the activation of DSA by the addition of Mn. This can be explained by the active interaction and reorientation of C atoms of Mn-C pairs in the 22Mn steel.[35]

C. *Effect of Al Addition on Deformation Behavior*

The grain size of the 18Mn2Al steel is similar to that of the 18Mn steel, and the phase transformation does not occur, as reported in previous researches.[10,15,19] The addition of Al increases the yield strength, and decreases the ultimate tensile strength and elongation, as shown in Table I. The increase in yield strength is explained by the solid solution hardening effect due the addition of Al.[46] The decrease in ultimate tensile strength is explained by the suppression of twin formation due to the small addition of Al. Since the addition of 1 wt pct of Al raises the SFE by 7.8 mJ m^{-2}, the SFE

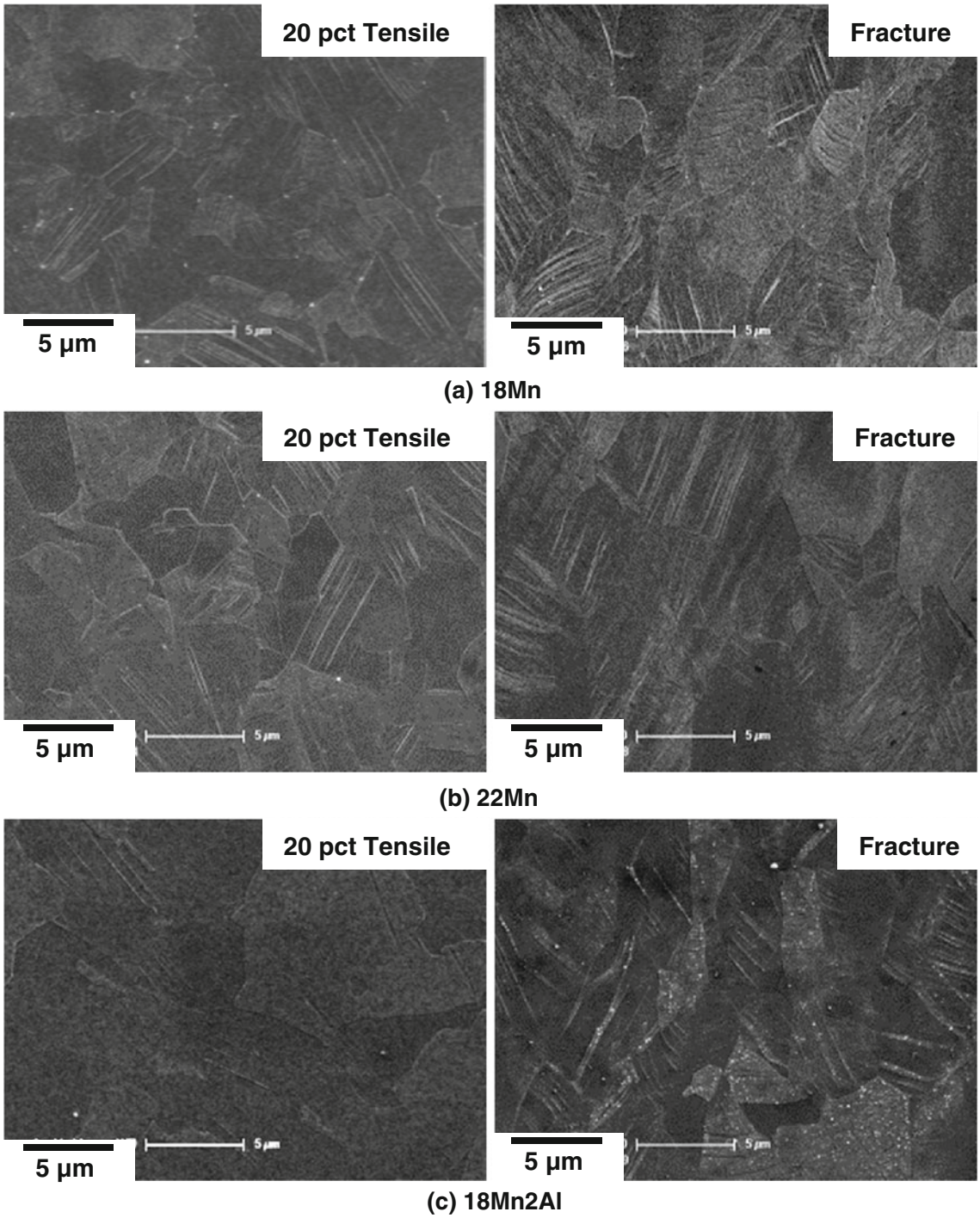

Fig. 10—SEM micrographs of the deformed microstructures of the (*a*) 18Mn, (*b*) 22Mn, and (*c*) 18Mn2Al steels after the tensile strain of 20 pct and fracture strain.

of the 18Mn2Al steel is about 34 mJ m^{-2}.[15] The increased SFE restrains the twin formation, while the cross slip is activated.[17–19,36] The restraint of the twin formation in the 18Mn2Al steel can be confirmed in Figure 10(c) and Table III. The elongation is reduced by the formation of some coarse AlN particles, as reported in the previous paper.[19]

It is interesting in the 18Mn2Al steel that the serration does not occur in the stress–time curves (Figures 6(a) and (b)), and that deformation bands are hardly formed as the deformation occurs homogeneously, although two weak bands are found in the final stage of deformation (Figures 5(e) and (f)). This is because the twin formation is restrained by high SFE (Figure 10(c)), and because the movement and reorientation of C atoms are reduced by the addition of Al due to decrease in carbon activity.[8,18] In the final stage of deformation prior to the fracture, the number of twins is increased by

the large deformation, which is enough to form bands. The 18Mn2Al steel has the better cup formability than the 18Mn and 22Mn steels without showing fluctuations in the load–displacement curve (Figures 2(a) and (b)) or cracking during the cup forming, although the tensile elongation is lower. Thus, the increase in SFE due to the Al addition lowers the load required for the cup forming, and restrains the band formation, thereby leading to the improvement of cup formability.

D. *Formation Behavior of Deformation Bands*

Average strain and strain rate of deformation bands increase almost linearly with increasing strain, as shown in Figures 8(a) and (b). This is because the amount of twins or stacking faults increases with increasing strain, and accelerates the interaction with C atoms.[35,39,44] The average width of bands rapidly increases in the initial deformation stage in the 18Mn and 22Mn steels because twins are readily formed and grown even in the initial stage (Figure 8(c)). This can be confirmed from the Table III and Figures 10(a) through (c), showing the twin formation in most of austenite grains even at the tensile strain of 20 pct. After the sufficient formation of twins, the average width of bands is maintained constant in a certain level. The average moving velocity of bands linearly decreases with increasing strain. This might be because the behavior of deformation bands is closely related with the movement of dislocations. Wijler and Van den Beukel[47] expressed the mobile dislocation density (ρ_m, unit:m^{-2}) existed inside deformation bands as:

$$\rho_m \approx \frac{\Delta\varepsilon_B}{b \cdot d_B}, \qquad [2]$$

where $\Delta\varepsilon_B$ refers to deformation band strain, b to dislocation burgers vector length (0.256 nm), and d_B to deformation band width. This equation is made under an assumption that the moving velocity of bands is same to the velocity of dislocations existed inside bands.[48] Using this equation, the mobile dislocation density was calculated, and is plotted as a function of strain in Figure 11. The mobile dislocation density increases with increasing strain. The increase in mobile dislocation density results in the restraint of movement of dislocations, and thus the moving velocity of bands is reduced as shown in Figure 8(d).

In the 18Mn2Al steel, only two deformation bands are formed in the final stage prior to fracture, but their average strain, strain rate, width, and moving velocity, and mobile dislocation density inside them are similar to those of the 18Mn and 22Mn steels (Figures 8(a) through (d) and 11). These results imply that bands are formed by the same formation mechanism of the 18Mn and 22Mn steels, although the Al addition effectively prevents the formation of deformation bands and serration phenomenon. In the three steels, thus, the 2nd last band moves upward, and the last band moves downward to reach the fracture (Figures 5(a) through (f)). This movement of the 2nd last band in the opposite moving direction indicates the change in the moving direction of dislocations, when assuming that the moving velocity of bands is same to the dislocation moving velocity. All deformation bands except the 2nd last band move continuously downward along the tensile loading direction as dislocations move downward in the same direction. This continuous moving behavior induces the pile-up of dislocations at grain or twin boundaries, and it subsequently increases the back stress. Accordingly, newly generated mobile dislocations cannot move in the same direction (downward direction), but move in the opposite direction which is an easy way, thereby leading to the movement of bands in the opposite direction (upward direction). Since these oppositely moving mobile dislocations influence already tangled dislocations,[49] it is likely that the stress–time curves of Figure 6(c) show somewhat different shapes of serrations. These results also confirm that the DSA is closely related with the movement of twinning partial dislocations.

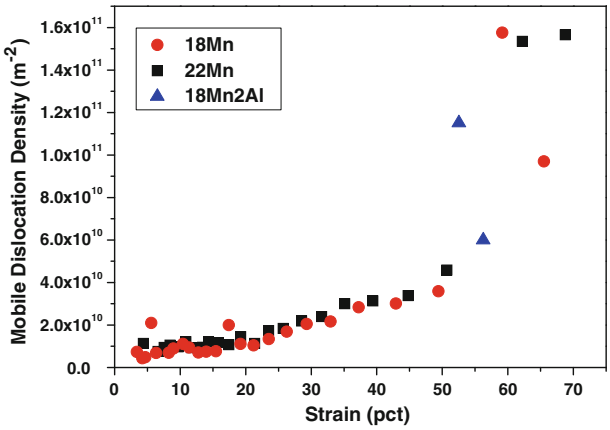

Fig. 11—Mobile dislocation density as a function of strain. The mobile dislocation density data were calculated from Eq. [2].

V. CONCLUSIONS

In the present study, the serration behavior of two high-Mn TWIP steels and an Al-added TWIP steel was examined by tensile tests, and was explained by the microstructural evolution including formation of deformation bands and twins.

1. The yield and ultimate tensile strengths decreased with increasing Mn content, while the elongation and cup formability were hardly varied, because the addition of Mn slightly raised the SFE and decreased the twin formation. In the Al-added steel, the decrease in tensile strength was explained by the increase in SFE due to the small addition of Al, as the increased SFE restrained the twin formation.
2. In room-temperature stress–strain curves of the three TWIP steels, serrations started in a fine and short shape, and their height and periodic interval increased with increasing strain. According to digital images of strain rate and strain obtained from a

vision strain gage system, deformation bands were initially formed at the upper region of the gage section, and moved downward along the tensile loading direction. The time when the band formation started was well matched with the time when one serration occurred in the stress–time curve. Serrations in stress–strain curves of the TWIP steels are closely related with the formation of deformation bands.

3. The serration behavior was generally explained by DSA, which was closely related with the formation of localized PLC deformation bands. In TWIP steels, DSA occurs because the reorientation of C atoms of Mn-C pairs obstructs the movement of twinning partial dislocations. Overall serration behavior of the 22Mn steel was similar to that of the 18Mn steel, while the number of bands and the fluctuation of strain hardening rate were increased by the activation of DSA due to the addition of Mn.
4. In the 18Mn2Al steel, deformation bands were hardly formed as the deformation occurred homogeneously, although only two weak bands were found in the final stage of deformation. This was because the twin formation was restrained, and because the movement and reorientation of C atoms were reduced by the addition of Al. Thus, the increase in SFE due to the Al addition lowered the load required for the cup forming, and suppressed the band formation, thereby leading to the improvement of cup formability.
5. Average strain and strain rate of deformation bands increased almost linearly with increasing strain. The average band width rapidly increased in the initial deformation stage, and then became saturated in the 18Mn and 22Mn steels because twins were readily formed and grown even in the initial stage. After the sufficient formation of twins, the average width of bands was maintained constant in a certain level. The average moving velocity of bands linearly decreased with increasing strain because the increase in mobile dislocation density led to the restraint of movement of dislocations.

ACKNOWLEDGMENTS

This work was supported by POSCO under a Contract No. 2009Y917. The authors would like to thank Professor Nack J. Kim of POSTECH for his discussion on serration phenomena. The authors would like to thank Soo-Hyun Joo for helping a vision strain gage system.

REFERENCES

1. O. Bouaziz, S. Allain, and C. Scott: *Scripta Mater*., 2008, vol. 58, pp. 484–87.
2. S. Allain, J.P. Chateau, and O. Bouaziz: *Mater. Sci. Eng*, 2004, vols. A387–89, pp. 143–47.
3. O. Bouaziz, S. Allain, C. Scott, P. Cugy, and D. Barbier: *Curr. Opin. Solid State Mater. Sci*., 2011, vol. 15, pp. 141–68.
4. I. Choi, Y. Park, D. Son, S.-J. Kim, and M. Moon: *Met. Mater. Int*., 2010, vol. 16, pp. 27–33.
5. N. Ma, T. Park, D. Kim, C. Kim, and K. Chung: *Met. Mater. Int*., 2010, vol. 16, pp. 427–39.
6. B.C. De Cooman, L. Chen, H.S. Kim, Y. Estrin, S.K. Kim, and H. Voswinckel: in *Microstructure and Texture in Steels*, 1st ed., A. Haldar, S. Suwas, and D. Bhattacharjee, eds., Springer, New York, NY, 2009, pp. 165–83.
7. M.N. Shiekhelsouk, V. Favier, K. Inal, and M. Cherkaoui: *Int. J. Plast*, 2009, vol. 25, pp. 105–33.
8. T. Shun, C.M. Wan, and J.G. Byrne: *Acta Metall*., 1992, vol. 40, pp. 3407–12.
9. J.G. Sevillano: *Scripta Mater*., 2009, vol. 60, pp. 336–39.
10. K.-G. Chin, C.-Y. Kang, S.Y. Shin, S. Hong, S. Lee, H.S. Kim, K.-H. Kim, and N.J. Kim: *Mater. Sci. Eng*., 2011, vol. A528, pp. 2922–28.
11. O. Grässel, L. Krger, G. Frommeyer, and L.W. Meyer: *Int. J. Plast*, 2000, vol. 46, pp. 1391–409.
12. O. Bouaziz and N. Guelton: *Mater. Sci. Eng*., 2001, vol. A319, pp. 246–49.
13. M. Koyama, T. Sawaguchi, K. Ogawa, T. Kikuchi, and M. Murakami: *Mater. Sci. Eng*., 2008, vol. A497, pp. 353–57.
14. A.S. Hamada, L.P. Darjalainen, and M.C. Somani: *Mater. Sci. Eng*., 2007, vol. A467, pp. 114–24.
15. J.E. Jin and Y.K. Lee: *Acta Mater*., 2012, vol. 60, pp. 1680–88.
16. J. Kim, S.-J. Lee, and B.C. De Cooman: *Scripta Mater*., 2011, vol. 65, pp. 363–66.
17. J.E. Jin, M. Jung, C.-Y. Lee, J. Jeong, and Y.-K. Lee: *Met. Mater. Int*., 2012, vol. 18, pp. 419–23.
18. B.K. Zuidema, D.K. Subramanyam, and W.C. Leslie: *Metall. Trans. A*, 1987, vol. 18A, pp. 1629–39.
19. S. Hong, S.Y. Shin, H.S. Kim, S. Lee, S.-K. Kim, K.-G. Chin, and N.J. Kim: *Metall. Mater. Trans. A*, 2012, vol. 42A, pp. 1870–83.
20. K.-T. Park, G. Kim, S.K. Kim, S.W. Lee, S.W. Hwang, and C.S. Lee: *Met. Mater. Int*., 2010, vol. 16, pp. 1–6.
21. M.R. Berrahmoune, S. Berveiller, K. Inal, and E. Patoor: *Mater. Sci. Eng*., 2006, vols. A438–440, pp. 262–66.
22. L. Chen, H.S. Kim, S.K. Kim, and B.C. De Cooman: *ISIJ Int*., 2007, vol. 47, pp. 1804–12.
23. J. Kim, L. Chen, H.S. Kim, S.-K. Kim, Y. Estrin, and B.C. De Cooman: *Metall. Mater. Trans. A*, 2009, vol. 40A, pp. 3147–58.
24. A. Roth, T.A. Lebedkina, and M.A. Lebyodkin: *Mater. Sci. Eng*., 2012, vol. A539, pp. 280–84.
25. T.A. Lebedkina, M.A. Lebyodkin, J.P. Chateau, A. Jacques, and S. Allain: *Mater. Sci. Eng*., 2009, vol. A519, pp. 147–54.
26. G.E. Dieter: in *Mechanical Metallurgy*, 3rd ed., McGraw-Hill Inc., New York, 1990.
27. L.H. De Almeida, I. Le May, and P.R.O. Emygdio: *Mater. Charact*., 1998, vol. 41, pp. 137–50.
28. A.H. Cottrell: *Trans. Metall. Soc. AIME*, 1958, vol. 212, pp. 192–202.
29. K.S.B. Rose and S.G. Glover: *Acta Metall*., 1966, vol. 14, pp. 1505–16.
30. G. Dini, A. Najafizadeh, R. Ueji, and S.M. Monir-Vaghefi: *Mater. Des*., 2010, vol. 31, pp. 3395–402.
31. B.X. Huang, X.D. Wang, Y.H. Rong, L. Wang, and L. Jin: *Mater. Sci. Eng*., 2006, vol. A438, pp. 306–40.
32. E. Bayraktar, F.A. Khalid, and C. Levaillant: *J. Mater. Process. Technol*., 2004, vol. 147, pp. 145–54.
33. S. Vercammen: Ph.D. Thesis, Katholieke Universiteit, Leuven, Belgium, 2004.
34. J. Chipman and E. Brush: *Trans. TMS AIME*, 1986, vol. 242, pp. 35–41.
35. W.S. Owen and M. Grujicic: *Acta Mater*., 1998, vol. 47, pp. 111–26.
36. V. Gerold and H.P. Karnthaler: *Acta Metall*., 1989, vol. 37, pp. 2177–83.
37. T.S. Kê and C.M. Wang: *Sci. Sin*., 1955, vol. 4, pp. 501–18.
38. V. Kandarpa and J.W. Spretnak: *Trans TMS AIME*, 1969, vol. 245, pp. 1439–42.
39. Y.N. Dastur and W.C. Leslie: *Metall. Trans. A*, 1981, vol. 21A, pp. 749–59.
40. H. Tanimoto: Ph.D. Thesis, Osaka University, Japan, 1990.
41. P.H. Alder, G.B. Olson, and W.S. Owen: *Metall. Trans. A*, 1986, vol. 17A, pp. 1725–37.

42. L.J. Cuddy and W.C. Leslie: *Acta Metall.*, 1972, vol. 20, pp. 1157–67.
43. V. Kandarpa and J.W. Spretnak: *Trans. Metall. Soc. AIME*, 1969, vol. 245, pp. 1439–42.
44. S.-J. Lee, J.K. Kim, S.N. Kane, and B.C. De Cooman: *Acta Mater.*, 2011, vol. 59, pp. 6809–19.
45. S. Allain, J.P. Chateau, O. Bouaziz, S. Migot, and N. Guelton: *Mater. Sci. Eng.*, 2004, vols. A387–89, pp. 158–62.
46. O. Grässel, G. Frommeyer, C. Derder, and H. Hofmann: *J. Phys. IV*, 1997, vol. 7, pp. 383–88.
47. A. Wijler and A. Van den Beukel: *Scripta Metall.*, 1970, vol. 4, pp. 705–08.
48. R. Sandstrom and R. Lagneborg: *Scand. J. Metall.*, 1974, vol. 3, pp. 205–11.
49. K. Ahn, D. Yoo, M.H. Seo, S.-H. Park, and K. Chung: *Met. Mater. Int.*, 2009, vol. 15, pp. 637–47.